(Received 21 June 2025, Accepted 3 August 2025, Scheduled 24 August 2025)

Low-frequency Dual-Port Microwave Sensor Based on CSRR and Electric Field Coupled for Precise Permittivity Detection in Biological Samples

Muhammad N. Kusumah[1], Syah Alam[1,*], Indra Surjati[1], Lydia Sari[1], Yuli K. Ningsih[1], Fitri K. Sari[1], Teguh Firmansyah[2], Noor A. Shairi[3], and Zahriladha Zakaria[3]

[1]*Department of Electrical Engineering, Universitas Trisakti, West Jakarta 11440, Indonesia*
[2]*Department of Electrical Engineering, Universitas Sultan Ageng Tirtayasa, Banten 42117, Indonesia*
[3]*Faculty of Electronic and Computer Engineering and Technology, Universiti Teknikal Malaysia Melaka, 76100, Malaysia*

ABSTRACT: This paper presents the development of a low-frequency dual-port microwave sensor designed for permittivity detection in both solid and biological materials. The sensor integrates a circular split-ring resonator (CSRR) with an electric field coupled (ELC) structure on a planar dielectric substrate, resulting in a compact and simple architecture that supports ease of fabrication and low-cost implementation. Operating at a resonant frequency of 0.86 GHz, the sensor is particularly suitable for characterising biological samples such as meat, fish, squid, and chicken, as lower frequencies offer deeper penetration and better interaction with high-loss biological tissues. Validation through full-wave simulation and experimental measurement confirms the sensor's capability to detect permittivity variations across a wide range of materials. A polynomial fitting model is employed to extract permittivity values based on resonance frequency shifts, achieving accurate results with a maximum error below 7% and overall accuracy exceeding 93%. The device demonstrates reliable performance in estimating permittivity values from $\varepsilon_r = 1$–9.8, including unknown biological samples with normalized sensitivity of 0.02% and frequency detection resolution 0.019 GHz. Measurements show clear frequency shifts that correlate with dielectric changes, and the experimental results align closely with the simulation data. The simple structure of the sensor also supports straightforward integration with common measurement instruments such as vector network analysers, making it practical for real-time monitoring and portable applications. The low operating frequency combined with the straightforward design provides an effective solution for applications requiring the permittivity detection of lossy, heterogeneous, or biological materials. This work contributes a feasible and efficient sensor platform for the use in medical diagnostics, food quality inspection, and other industrial contexts where reliable, low-cost dielectric sensing is essential.

1. INTRODUCTION

Microwave sensors are often used for material characterization in various fields, such as food manufacturing, medical applications, and industrial environments [1–3]. The microwave sensor will respond to the material depending on its permittivity [4, 5]. The tested solid material (Sample Under Test) is placed in the highest electric field in the resonator structure, which is the sensing area of the microwave sensor [6, 7]. Microwave sensors have the advantage of high performance in terms of accuracy and sensitivity [8]. In the microwave sensor, the parameters that need to be considered to determine the performance of microwave sensors are frequency detection resolution (FDR), average accuracy, and normalized sensitivity (NS).

Previous works are mostly confined to solid, semi-solid materials [9, 10] and lack adaptability for organic or biological samples. A previous work [9] on the detection of solid material uses a resonator structure based on a U-shaped resonator, yielding FDR of 0.009 and 0.043, average accuracies of 99.02% and 96.44%, and NS values of 1.072% and 1.150% for each area, respectively. Another work [10] for detecting semi-solid material using a triple-ring CSRR structure sensor yields an FDR of 0.042, an average accuracy of 96%, and an NS of 0.003%. However, they are limited to solid materials with known permittivity and do not support the detection of biological materials such as meat, fish, squid, and chicken. To address these limitations, this work proposes a novel dual-port microwave sensor design based on a circular split ring resonator with an electric field coupling mechanism. The circular split ring resonator (CSRR) structure of microwave sensors provides a flexible platform for building topological structures with complex coupling distributions, enabling electromagnetic wave control [11, 12]. In addition, the utilization of the resonator's electric field coupled (ELC) structure is used to create an inductive arm and concentrate the electric field in the specific sensing area location. This makes them highly sensitive to dielectric perturbations, such as changes in permittivity near the sensor [13]. Moreover, to detect the permittivity of biological materials, the designed microwave sensor will have a low frequency. Low frequencies have more penetration inside the tissues than higher frequencies due to the inherent conductivity of biological tissues [14].

* Corresponding author: Syah Alam (syah.alam@trisakti.ac.id).

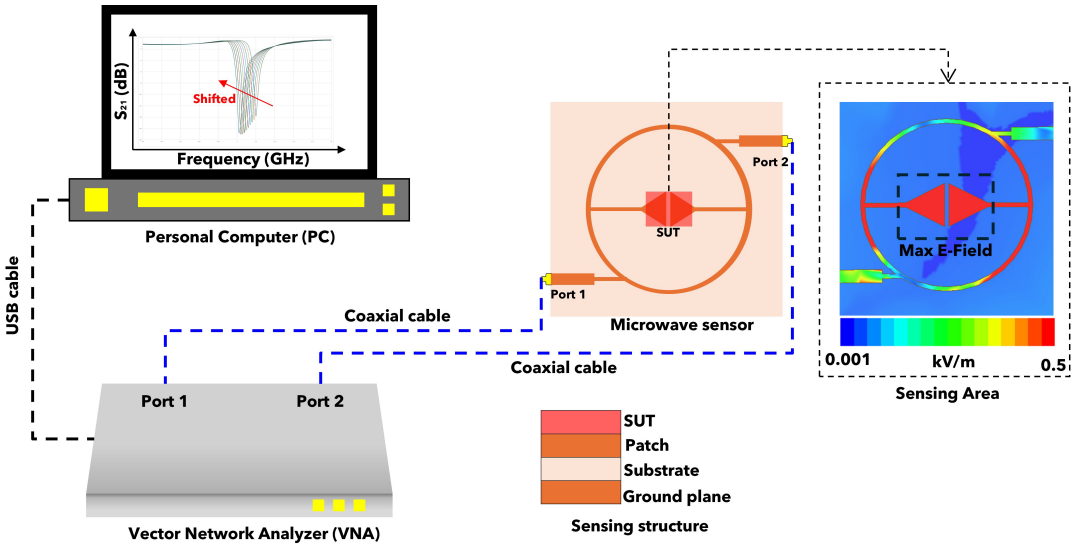

FIGURE 1. Proposed scenario for permittivity detection based on a microwave sensor.

The main contributions of this paper include the introduction of a novel planar resonator design that can detect the permittivity of solid materials and biological materials. The proposed sensor features a compact and straightforward architecture based on complementary split-ring resonator (CSRR) and electric field coupled (ELC) structures, which simplifies the fabrication process and reduces implementation costs.

Moreover, the design operates at a relatively low frequency, making it well suited for characterising biological materials due to improved field interaction. This combination of structural simplicity, affordability, and frequency suitability offers a promising solution for practical microwave sensing applications.

2. WORKING PRINCIPLE OF MICROWAVE SENSOR FOR PERMITTIVITY DETECTION

Figure 1 presents the proposed measurement setup for permittivity detection utilizing a microwave sensor. The system comprises three main components: a Vector Network Analyzer (VNA), a microwave resonator-based sensor, and a personal computer (PC) for data visualisation and analysis.

The VNA, connected to the sensor via coaxial cables at Port 1 and Port 2, injects and receives microwave signals across a frequency range. The PC receives the scattering parameters (S-parameters), particularly S_{21}, via a USB interface. Any variation in the dielectric properties of the Sample Under Test (SUT) placed on the sensor leads to a shift in the resonance frequency, as illustrated in the S-parameter plot shown on the PC display. The red-shifted curve indicates the effect of permittivity change.

The microwave sensor comprises a resonator featuring a circular split ring structure and an electric field coupled design, fabricated on a dielectric substrate with a conductive patch and a ground plane. The sensing mechanism relies on the strong electric field concentration within a designated sensing area, as depicted in the electric field distribution map. This concentration ensures high sensitivity to variations in the permittivity of the SUT. The sensing area of the proposed sensor was determined based on the location of the maximum electric field of the resonator, which is concentrated at the centre of the structure featuring a back-arrow structure. This back-arrow structure was introduced to enhance both the electric field intensity and the effective sensing area of the sensor.

Figure 2 provides a detailed structural view of the planar microwave sensor used for permittivity detection. The sensor is fabricated on a dielectric substrate with a thickness h of 1.6 mm that includes a resonator, feedline, and connectors for signal transmission.

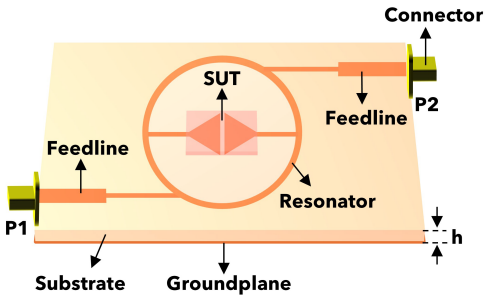

FIGURE 2. Detailed structure of the planar microwave sensor.

The SUT is placed directly above the resonator, where the electric field is maximally confined. The resonator is coupled to the input and output ports (P1 and P2) via feedlines, which facilitate microwave transmission. These feedlines are connected to SMA connectors, enabling integration with the VNA.

The resonator geometry and its interaction with the SUT are critical to the sensor's functionality. When the SUT is introduced, it perturbs the resonant frequency due to its dielectric properties, enabling permittivity estimation based on the observed frequency shift.

The combination of the electromagnetic field simulation and physical sensor layout ensures a highly sensitive and compact solution for material characterisation in the microwave regime.

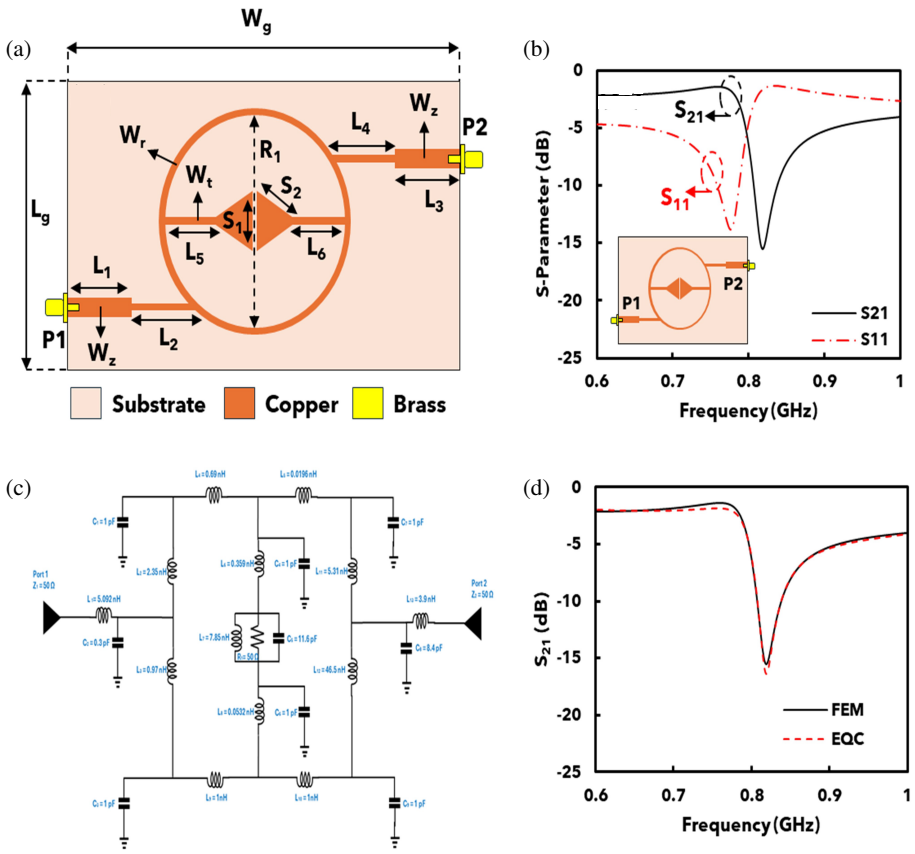

FIGURE 3. Design and analysis of the proposed microwave sensor; (a) geometry and dimensional parameters of the proposed sensor, (b) simulation setup for S_{11} and S_{21} measurement, (c) equivalent circuit model, (d) simulated reflection coefficient (S_{21}) of the proposed sensor.

3. DESIGN AND SIMULATION

3.1. Design and Structure of Proposed Microwave Sensor

The proposed microwave sensor is designed using an FR4 type substrate with dielectric constant (ε_r) of 4.3, loss tan ($\tan\delta$) of 0.0265, and thickness (h) of 1.6 mm. Furthermore, the sensor is modelled and simulated using High Frequency Structure Simulator (HFSS) 15.0 to observe the performance of the proposed resonator. The proposed sensor is developed based on a resonator with a two-port configuration (P1 and P2) of an impedance of 50 Ω connected to a microstrip transmission line. In addition, the equivalent circuit with R, L, and C components is also proposed and compared with Finite Element Modelling (FEM) simulation to confirm the performance of the proposed resonator. The structure and simulation results of the proposed sensor are shown in Fig. 3.

Figure 3(a), the physical layout of the sensor, comprising a planar resonator structure implemented on a dielectric substrate (light pink). The conductive traces, made of copper (orange), include a back-arrow structure (S_1 and S_2) symmetrically positioned inside a circular resonator of radius R_1. These patches are connected to feedlines (L_1–L_6), which guide the radio frequency (RF) signal between Port 1 (P1) and Port 2 (P2). The substrate is supported by a ground plane, and brass connectors are used for interfacing with external measurement equipment. The arm length of the CSRR structure for a given resonant frequency can be determined using Equation (1) as follows [15]:

$$l = \frac{c}{2\sqrt{\varepsilon_{eff}}} \times \frac{1}{f_r} \tag{1}$$

where l is the total length of the resonator in millimeters (mm), c the speed of light in free space (approximately 3×10^8 m/s), ε_{eff} the effective permittivity of the substrate, and f_r the desired resonant frequency in gigahertz (GHz).

The substrate dimensions and dimensional details on the copper parts of the microwave sensor are provided in Table 1.

TABLE 1. Dimensions of the proposed microwave sensor.

Parameters	Dimension (mm)
$W_g - L_g$	50
W_z	3
$L_{1,3}$	10
$L_{2,4}$	4.5
$L_{5\text{-}6}$	14.5
S_1	10
S_2	9
W_{r-t}	1
R_1	40

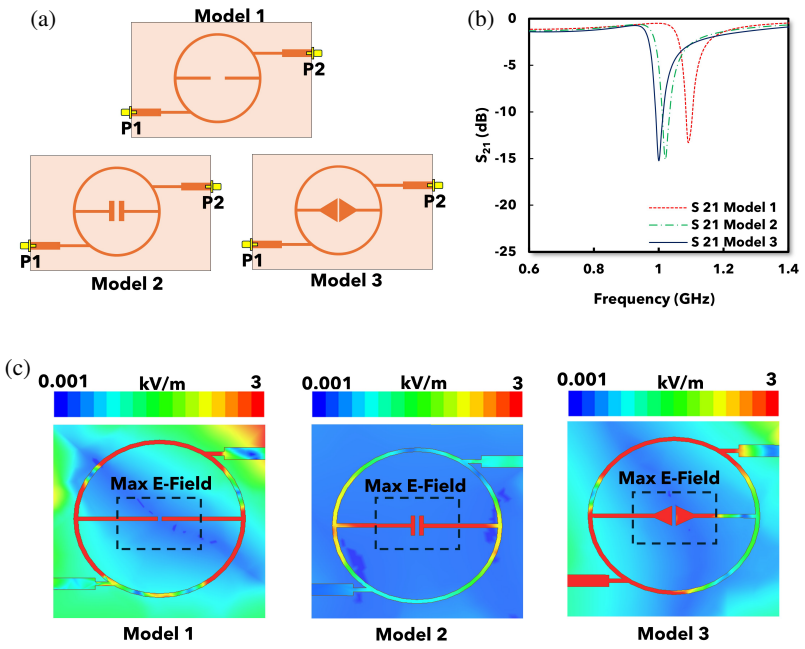

FIGURE 4. Comparison of resonator structures and electric field distributions; (a) development model of the microwave sensor, (b) simulated S_{21} parameters of the three structures, (c) electric field distribution of the microwave sensor.

Figure 3(b) shows the S-parameter (scattering parameter) response of the sensor obtained from full-wave simulation, where S_{21} and S_{11} are plotted over the frequency from 0.6 GHz to 1 GHz. Parameter S_{21} is at a frequency of 0.82 GHz, and parameter S_{11} is at a frequency of 0.78 GHz. This finding indicates that the proposed resonator has low-pass characteristics. The inset highlights the sensor structure with a back-arrow design and the location of the excitation ports (Port 1 and Port 2). The dip in S_{11} at the same frequency confirms proper impedance matching. Additionally, the graph demonstrates the sensor's low-pass filter behaviour, as it exhibits high transmission at lower frequencies, followed by a rapid attenuation beyond the resonance point. This filtering effect shows that the structure effectively allows low-frequency signals to pass while suppressing higher-frequency components.

Moreover, Fig. 3(c) illustrates the lumped-element equivalent circuit (EQC) model that replicates the electromagnetic behaviour of the designed resonator structure. The circuit comprises multiple inductors and capacitors strategically arranged to emulate the distributed effects of the physical resonator. Notably, each section of the resonator is represented by series and parallel RLC components to account for both the transmission line characteristics and localized resonant phenomena. The use of standard 50 Ω ports (Port 1 and Port 2) ensures impedance matching with the external system. This circuit abstraction provides a practical approach for initial design estimation, enabling efficient parametric tuning and analytical insight into the resonator's performance. Details of each RLC component in the EQC circuit are provided in Table 2.

Furthermore, Fig. 3(d) compares the simulated transmission coefficient S_{21} responses obtained from the finite element method (FEM) full-wave simulation and EQC model. As shown, both results display a prominent resonance dip occurring at approximately the same frequency, affirming that the EQC model accurately captures the essential resonant characteristics of the physical structure. While excellent agreement is observed in the vicinity of the resonance, minor discrepancies appear at off-resonance frequencies. These deviations can be attributed to idealizations in the EQC, such as neglecting higher order parasitic and radiation effects, which are inherently captured in the FEM simulation. Nevertheless, the overall correlation validates the efficacy of the EQC model as a reliable and computationally efficient surrogate for the full-wave model.

TABLE 2. Details of the RLC component for equivalent circuit of proposed sensor.

Component	Value	Component	Value
$Z_{1\text{-}2}$	50 Ω	L_8	0.0532 nH
R_1	50 Ω	$L_{9\text{-}10}$	1 nH
L_1	5.092 nH	L_{11}	5.31 nH
L_2	2.35 nH	L_{12}	46.5 nH
L_3	0.97 nH	L_{13}	3.9 nH
L_4	0.69 nH	$C_{1,3,4,6,7,9}$	1 pF
L_5	0.0196 nH	C_2	0.3 pF
L_6	0.359 nH	C_5	11.6 pF
L_7	7.85 nH	C_8	8.4 pF

3.2. Development of Microwave Sensor

The proposed sensor is developed in three different models to observe the performance and determine the location of the sensing area of the sensor as shown in Fig. 4(a). Model 1 represents the base design, consisting of a standard circular resonator without any added structures in the sensing area. Model 2 incor-

porates a narrow strip placed centrally within the sensing area, designed to alter the electric field distribution and improve sensitivity. In contrast, Model 3 introduces a back-arrow-shaped structure in the same region, intended to maximise electric field confinement and strengthen capacitive coupling with the material under test. All three models share the same overall layout, including coaxial feeding at Port 1 and Port 2, ensuring a fair comparison of their respective electromagnetic performances.

Moreover, Fig. 4(b) represents the transmission coefficient (S_{21}) of each model plotted over the frequency range of 0.6 to 1.4 GHz. The results reveal clear performance differences among the models. In Model 1, the resonant frequency is 1.09 GHz, Model 2 shifted to 1.02 GHz, and Model 3 shifted to 1 GHz. Model 1 shows a shallow resonant dip with relatively wide bandwidth, indicating limited sensitivity and weaker resonance behaviour. Model 2, enhanced by the inclusion of the central strip, displays a more pronounced resonant notch, signifying improved field interaction and narrower bandwidth. Model 3, featuring a back-arrow structure, exhibits the deepest and sharpest S_{21} dip among all models, confirming a stronger resonance and higher sensitivity. The resonant frequency shifts and resonance depth observed validate the influence of structural loading in the sensing area, with Model 3 demonstrating superior performance due to its optimised field confinement and coupling effects.

The electric field distribution of each model at its respective resonant frequencies is visualised in Fig. 4(c). The field maps show the magnitude of the electric field in a colour-coded scale ranging from 0.001 kV/m to 3 kV/m. In Model 1, the electric field is relatively dispersed, with moderate intensity around the sensing area. Model 2 shows a more focused electric field concentrated near the strip structure, leading to improved interaction with the sample. Model 3 exhibits the highest electric field intensity and the most localised field distribution, especially around the back-arrow structure. This strong field confinement directly correlates with the sensor's enhanced performance in terms of sensitivity and permittivity detection. The simulation results confirm that introducing tailored structures within the resonator's sensing region significantly impacts the electromagnetic behaviour, making Model 3 the most efficient design for high-resolution sensing applications.

3.3. Simulation of Microwave Sensor for Detection of Permittivity in the Range 1--10

Next, a simulation of sample permittivity detection is proposed using HFSS 15.0 where the sample is placed directly above the surface of the sensing area. Fig. 5(a) presents the sensor configuration where a rectangular Sample Under Test (SUT) with dimensions $15 \times 10 \times 1$ mm, labeled a, b, and thickness t, is placed over the sensing area of the resonator. The resonator structure is realised using a copper pattern on a dielectric substrate with a ground plane beneath. The resonator is excited by two feedlines connected to Port 1 (P1) and Port 2 (P2). The high electric field concentration in the sensing region ensures strong interaction with the dielectric properties of the SUT.

Moreover, Fig. 5(b) shows the simulated transmission coefficient S_{21} over the frequency range of 0.5–1.0 GHz for ten different relative permittivity values ε_r ranging from 1 to 10. When the value of $\varepsilon_r = 1$, the resonance frequency is 0.83 GHz and continues to shift until $\varepsilon_r = 10$, and the resonance frequency shifts to 0.64 GHz. As ε_r increases, the resonance frequency of the sensor systematically shifts toward lower frequencies. This downshift is attributed to the increase of the sensor effective capacitance, which subsequently decreases the resonance frequency.

Next, Fig. 5(c) and Fig. 5(d) offer polynomial fits correlating the permittivity and corresponding resonance frequency while in Fig. 5(c), the second-order polynomial equation is as follows in Equation (2):

$$\varepsilon_r = 109.72(f_r)^2 - 208.05(f_r) + 98.112 \quad (2)$$

where f_r is the resonant frequency (GHz), and ε_r is the relative permittivity. This equation exhibits a strong correlation, and $R^2 = 1$ accurately models permittivity as a function of frequency. Conversely, Fig. 5(d) provides the inverse relationship where frequency is plotted against permittivity with a similarly strong fit shown in Equation (3) as follows:

$$f_r = 0.001(\varepsilon_r)^2 - 0.032(\varepsilon_r) + 0.8585 \quad (3)$$

Based on Fig. 5(d), the polynomial equation has a high accuracy with $R^2 = 0.9992$. These relations can be employed for permittivity extraction of unknown samples. Using the polynomial equation to determine the permittivity value based on the resonant frequency shift in a sample whose permittivity is known using software simulation, the error value and accuracy of the microwave sensor can be obtained when the permittivity value is detected with an average accuracy of 99.69%.

Furthermore, Fig. 5(e) examines the frequency shift Δf due to changes in permittivity $\Delta\varepsilon_r$. The curve follows a second-order polynomial fit equation, as in Equation (4):

$$\Delta f = -0.001(\Delta\varepsilon_r)^2 + 0.0299(\Delta\varepsilon_r) + 0.0029 \quad (4)$$

where Δf stands for frequency shift (GHz), and $\Delta\varepsilon_r$ is the change in relative permittivity. The R^2 value of 0.9992 indicates that the sensor has a high accuracy to detect permittivity values of the samples. The near-quadratic nature of the curve suggests a nonlinear sensing behaviour, which is often observed in high-sensitivity resonator designs.

In addition, Fig. 5(f) shows the variation of frequency detection resolution (FDR), a normalized sensitivity metric, concerning $\Delta\varepsilon_r$. Based on the simulation results as shown in Fig. 5(e) and Fig. 5(f), the maximum ΔF and FDR of the proposed sensor for the permittivity range of 1–10 are 0.19 GHz and 0.036 GHz/$\Delta\varepsilon_r$, respectively. These findings indicate that the proposed sensor has high performance for detecting the permittivity of solid materials.

Furthermore, to observe the accuracy of the sensor with different sample dimensions, a simulation was proposed by placing samples with four different dimensions in the sensor's sensing area, as shown in Fig. 6.

The accuracy of the sensor with different sample dimensions is determined by observing the correlation between the resonance frequency and permittivity of the sample represented by the polynomial equation shown in Fig. 6. Based on the simulation results with four different sample dimensions, the

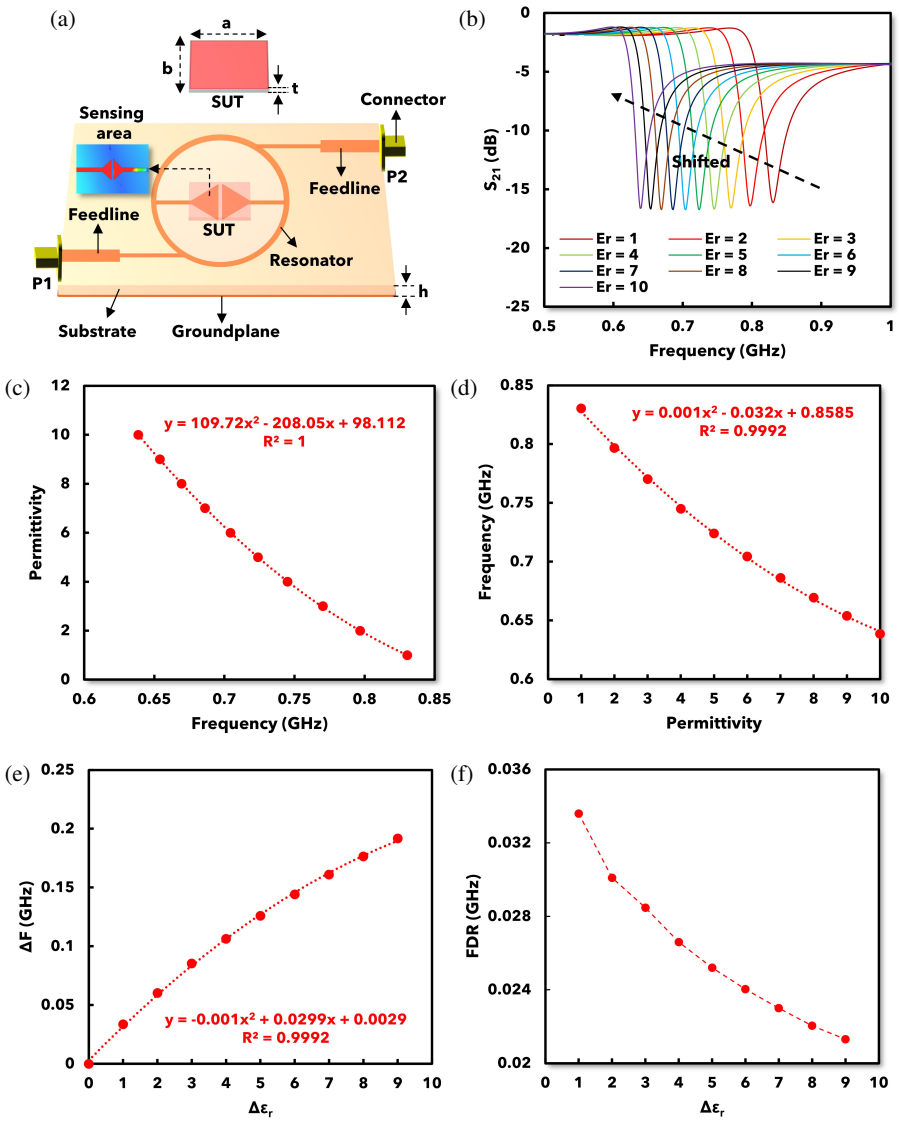

FIGURE 5. Sensor performance and calibration analysis; (a) simulation setup from proposed sensor, (b) simulated S_{21} for ε_r of 1–10, (c) polynomial equation to determine ε_r, (d) polynomial equation to determine f_r, (e) polynomial equation to determine Δf, (f) correlation between FDR and $\Delta\varepsilon_r$.

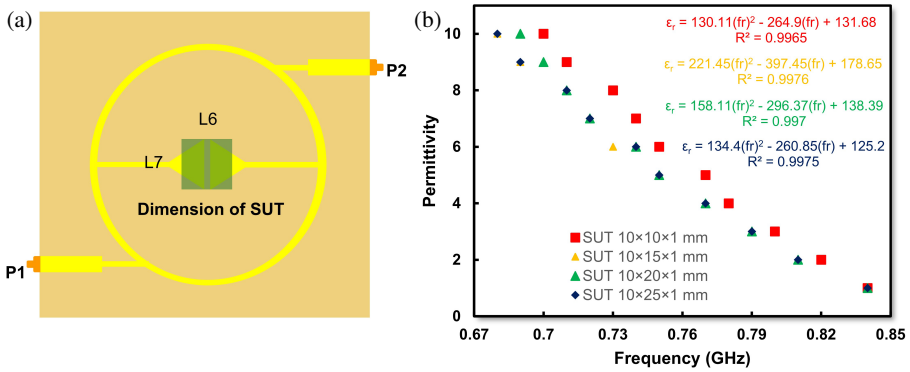

FIGURE 6. Simulation of proposed sensor with different sample dimensions; (a) dimension of SUT, (b) fitting curve for different sample dimensions.

proposed sensor has a high accuracy in the range of 97.26%–97.98% while the maximum FDR and normalized sensitivity are 0.022 GHz and 0.241% as shown in Table 3. These findings indicate that the sample dimensions do not have a significant impact on the accuracy of the proposed sensor. From these results, the best accuracy is obtained at sample dimensions of

TABLE 3. Accuracy of proposed sensor with different sample dimensions.

Sample	FDR (GHz)	Average Accuracy (%)	Normalized Sensitivity (%)
SUT 10 × 10 × 1 mm	0.022	97.59	0.241
SUT 10 × 15 × 1 mm	0.022	97.98	0.235
SUT 10 × 20 × 1 mm	0.022	97.51	0.220
SUT 10 × 25 × 1 mm	0.022	97.26	0.235

10 mm × 15 mm × 1 mm with an accuracy of 97.98%. Therefore, this sample dimension is used in the measurement process referring to the simulation results with the best accuracy.

4. VALIDATION AND MEASUREMENT

4.1. Measurement Process of the Proposed Microwave Sensor

Validation and measurement of the sensor were carried out in the laboratory using a Vector Network Analyzer (VNA) with a frequency range of 0.6–1 GHz, a sweep frequency of 0.001 GHz, and an ambient temperature of 25°C. Fig. 7(a) shows the experimental setup, where the sensor is connected to a VNA through coaxial cables linked to Port 1 and Port 2. The SUTs include both known dielectric materials (labeled A–E) and various biological tissues such as squid, chicken, fish, and beef. These materials are positioned on the sensing area of the sensor as depicted in the image. For each sample, the dimensions are the same and adjusted to the simulation carried out of 15 mm × 10 mm × 1 mm, both samples with known permittivity and biological samples to be tested. In this paper, the values of samples with known permittivity are shown in Table 4.

TABLE 4. Sample of known permittivity.

Labelled	SUT	ε_r
n/a	Vacuum	1
E	RO-5880	2.2
B	RO-4003C	3.55
D	FR-4	4.3
C	RO-3006	6.15
A	TM-10	9.8

Figure 7(b) presents a comparison between the simulated and measured transmission coefficients S_{21} of the sensor. The resonance frequency of the measured curve closely aligns with the simulated results, validating the sensor's design. A minor discrepancy is observed, which may be attributed to fabrication tolerances, connector losses, or imperfect sample placement. Furthermore, Fig. 7(c) displays the measured S_{21} responses for various dielectric substrates, including vacuum, RO3006, RO4003C, FR4, TM10, and RO5880. The plot shows a systematic leftward shift in resonance frequency with increasing permittivity, consistent with electromagnetic theory. In the condition without sample (Vacuum), the resonant frequency is 0.86 GHz, and after placing the sample with permittivity $\varepsilon_r = 2.2$, the resonant frequency shifts to 0.83 GHz and continues to shift until the permittivity $\varepsilon_r = 9.8$, to 0.72 GHz. The downshift indicates stronger interaction between the electric field and higher-permittivity materials.

Next, the correlation between permittivity and the corresponding measured resonance frequency of proposed sensor is shown in Fig. 7(d). A third-order polynomial regression is used to model the trend shown in Equation (5) as follows:

$$\varepsilon_r = -1178.1(f_r)^3 + 3036.8(f_r)^2 - 2651.8(f_r) + 784.63 \quad (5)$$

Based on Fig. 7(d), the polynomial equation has a high coefficient of determination $R^2 = 0.998$, indicating excellent curve fitting. This model enables precise permittivity extraction from measured frequency data. Using the polynomial equation, the error value and accuracy of the microwave sensor can be known when measuring samples that have known permittivity values. Moreover, Table 5 provides the resonant frequency shift in each sample whose permittivity is known, along with the error value and accuracy when each sample is measured.

TABLE 5. Comparison of the known permittivity value and calculated permittivity.

f_r (GHz)	ε_r	ε_r cal	Error	Accuracy
0.86	1	0.97	2.59%	97.41%
0.83	2.2	2.07	6.12%	93.88%
0.80	3.55	3.45	2.93%	97.07%
0.78	4.3	4.49	4.45%	95.55%
0.76	6.15	5.93	3.56%	96.44%
0.72	9.8	9.78	0.23%	99.77%

Table 5 presents the validation results of the microwave sensor's capability to extract permittivity values from measured resonance frequencies. The data shown are based on a polynomial model with a high coefficient of determination ($R^2 = 0.998$), which indicates excellent curve fitting between the measured resonance frequency and the known permittivity values. This model enables accurate estimation of permittivity (ε_r) from the measured frequency shift. The table compares the known permittivity values of various samples with the calculated values, and it also provides the corresponding error percentages and accuracy. For example, the sample with a known permittivity of 9.8 shows a calculated value of 9.78, resulting in a very low error of 0.23% and a high accuracy of 99.77%. Overall, the results in Table 5 confirm that the proposed method delivers accurate permittivity extraction, with all samples achieving accuracy above 93.8%, validating the reliability of the sensor system.

Microwave sensor parameters include frequency detection resolution (FDR) and normalized sensitivity (NS), each of which plays an important role in determining sensor performance. The relationship between the change in resonant frequency and the permittivity value of the SUT is referred to as FDR, which can be calculated using Equation (6) as follows [16]:

$$FDR = \frac{\Delta f}{\Delta \varepsilon_r} \text{ (GHz)} \quad (6)$$

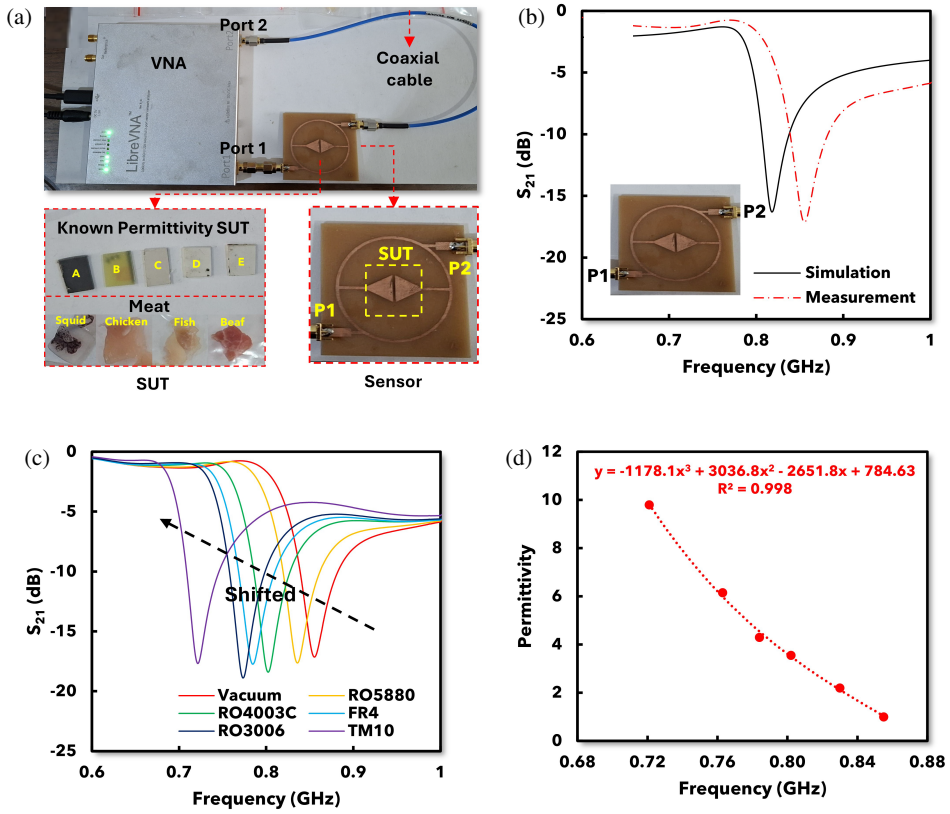

FIGURE 7. Experimental setup and validation using sample under test; (a) measurement setup with fabricated sensor, (b) comparison simulation and measurement of proposed sensor, (c) measured S_{21} response of the sensor with known permittivity samples, (d) graph of a polynomial equation to determine ε_r of known permittivity samples.

In Equation (6), Δf is the difference between the resonant frequency of the microwave sensor before the SUT is placed ($f_{unloaded}$) and that after the SUT is placed (f_{loaded}) while $\Delta\varepsilon_r$ is the difference between the highest permittivity and the reference permittivity. In general, the reference permittivity value used is vacuum with $\varepsilon_r = 1$ [17].

Normalized Sensitivity (NS) value can be calculated using Equation (7) as follows [18]:

$$NS = \frac{1}{\Delta\varepsilon_r} \times \left(\frac{f_{unloaded} - f_{loaded}}{f_{unloaded}} \right) \% \qquad (7)$$

Figure 8(a) shows the relationship between the frequency detection resolution (FDR) and the dielectric constant variation $\Delta\varepsilon_r$. FDR is calculated as the difference in resonant frequencies normalized by a reference frequency. The plot indicates a decreasing trend in FDR as $\Delta\varepsilon_r$ increases, highlighting reduced sensitivity at higher permittivity values. The nonlinear nature of this response suggests that frequency-based permittivity extraction is more accurate in low-to-mid permittivity ranges. Furthermore, Fig. 8(b) plots the absolute frequency shift Δf against $\Delta\varepsilon_r$, where a third-order polynomial regression is used to model the sensor's sensitivity curve, shown in Equation (8) as follows:

$$\Delta f = 7\times10^{-5}(\Delta\varepsilon_r)^3 - 0.0018(\Delta\varepsilon_r)^2 + 0.0257(\Delta\varepsilon_r) - 0.0011 \qquad (8)$$

Based on Fig. 8(b), the polynomial has $R^2 = 0.9976$, and it demonstrates high agreement between calculated and observed data. This curve can serve as a predictive model for identifying unknown permittivity from frequency responses. In addition, Fig. 8(c) presents a validation comparison between reference permittivity values ε_r (square markers) and those calculated by the proposed model (triangle markers). The close alignment between the reference and calculated data across the frequency spectrum confirms the sensor's accuracy. This comparison validates that the mathematical model used for permittivity extraction is suitable for both simulation and real-world data.

Furthermore, to observe the performance stability of the proposed sensor, repeatability measurement is proposed with several measurement processes. Moreover, Fig. 9 shows the repeatability measurement of the proposed sensor which was carried out 3 times.

From the measurement results, the sensor has a stable performance in detecting the permittivity of samples with known permittivity in the range of 1–9.8 as shown in Table 6. This finding indicates that the sensor has accuracy and stable performance in repeatability measurements.

4.2. Validation and Performance of the Microwave Sensor for Permittivity Detection of Biological Samples

Furthermore, permittivity detection of biological materials such as meat is proposed in this work by placing the sample on

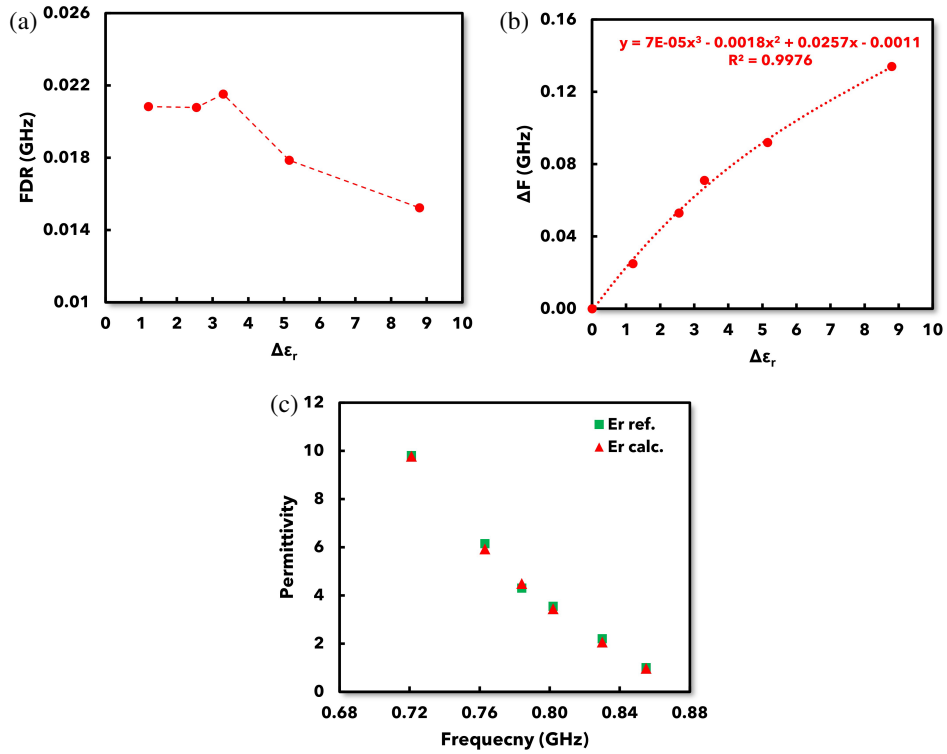

FIGURE 8. Evaluation of sensor performance for known permittivity samples; (a) graph correlation between FDR and $\Delta\varepsilon_r$, (b) graph of a polynomial equation to determine Δf, (c) comparison of measured and calculated permittivity values for known permittivity samples.

TABLE 6. Repeatability measurement from proposed sensor compared with known permittivity materials.

f_r (GHz)	ε_r ref	M1	M2	M3
0.86	1	0.97	0.96	0.98
0.83	2.2	2.07	2.06	2.07
0.80	3.55	3.45	3.44	3.46
0.78	4.3	4.49	4.47	4.48
0.76	6.15	5.93	5.91	5.92
0.72	9.8	9.78	9.76	9.77

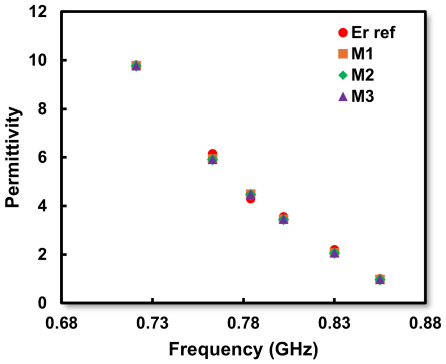

FIGURE 9. Repeatability measurement of proposed sensor with known permittivity in the range 1–9.8.

the surface of the sensing area of the sensor. The permittivity of the biological sample is determined using a polynomial equation obtained from the frequency response and permittivity of the sample with known permittivity. Fig. 10(a) illustrates the S_{21} responses of the sensor with biological tissues (fish, chicken, meat, and squid) placed over the sensing area. Similar to Fig. 7(c), the resonance frequency shifts depending on the permittivity of each biological sample. When the sensor is placed on bare plastic, the resonant frequency is at 0.85 GHz, and when the fish sample is placed, it shifts to a frequency of 0.79 GHz and for the chicken sample shifts to 0.69 GHz. The bare sensor (vacuum condition) shows the highest resonance frequency, while chicken, having higher water content, produces the lowest frequency due to higher permittivity.

Moreover, Fig. 10(b) illustrates the relationship between the resonant frequency and dielectric permittivity for various test samples, including fish, meat, chicken, and squid. The measured data points align closely with a fitted third-order polynomial regression (red dotted curve), which has been determined using samples with known permittivity from previous measurements. Materials with known permittivity are used as calibrators to obtain mathematical equations to determine the permittivity of samples with unknown permittivity. This regression model enables the estimation of unknown permittivity based on observed resonant frequency shifts. However, the polynomial fit is only valid up to a relative permittivity (ε_r) of 9.8. Therefore, permittivity values beyond this limit, including those of chicken meat, which exceed the model's range, cannot be accurately calculated using this equation. The overall result of calculating the permittivity value of biological samples is shown in Table 7.

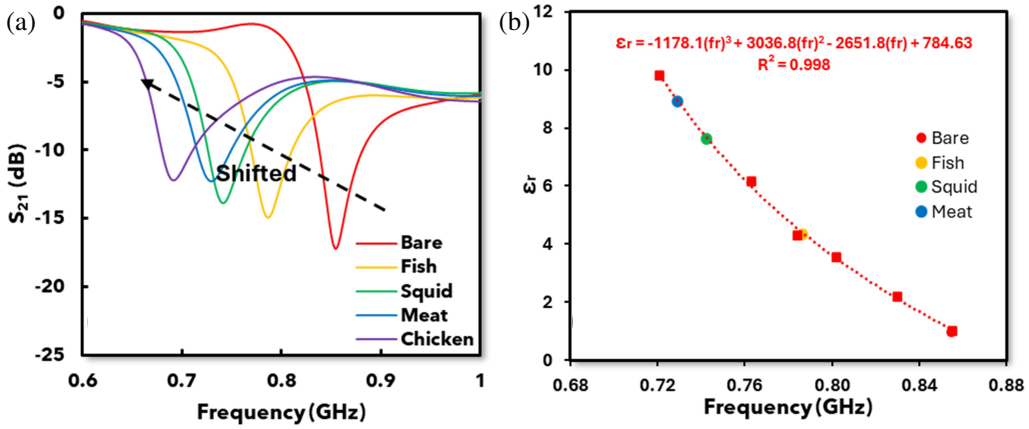

FIGURE 10. Microwave sensor response for various meat samples; (a) S_{21} response for different meat types, (b) polynomial fitting of permittivity (ε_r) as a function of resonant frequency shift.

TABLE 7. Permittivity value of the biological sample.

SUT	f_r (GHz)	ε_r Cal
Bare	0.85	0.99
Fish	0.79	4.34
Squid	0.74	7.64
Meat	0.73	8.91

5. COMPARISON WITH PREVIOUS WORK

In order to demonstrate the novelty of the proposed work, a fair comparison with previous work is proposed as shown in Table 8. The comparison is proposed by observing the method, resonance frequency, number of ports, performance of the sensor, and the type of sample detected.

In previous work [9], the designed microwave sensor has a resonator structure based on a U-shaped resonator with a resonant frequency of each sensing area in the resonator of 1.21 GHz and 2.10 GHz for the characterization of solid materials with a permittivity of 1 to 4.3. The characterized solid materials are air, RO5880, RO4003C, and FR4 with permittivities of 1, 2.2, 3.68, and 4.3, respectively. Based on the measurement and calculation of FDR values, the average accuracy and NS obtained in the first sensing area are 0.009, 99.02%, and 1.072%, while in the second sensing area are 0.043, 96.44%, and 1.150%.

In another previous work [10], the designed microwave sensor has a triple-rings CSRR structure with a resonant frequency of 2.5 GHz for the characterization of semi-solid materials with a permittivity of 1.0006 to 78.4. The characterized solid materials are empty tube, Turmeric, Java Turmeric, Black Turmeric, Mango Ginger, and DI Water with permittivities of 1.0006, 34.52, 45.6, 46.68, 59.61, and 78.4, respectively. Based on the measurement and calculation of FDR values, the average accuracy and NS obtained are 0.042, 96%, and 0.003%.

In previous work [19], the designed microwave sensor has a resonator structure based on a double split ring resonator with a resonant frequency of 2.45 GHz for the characterization of solid and liquid materials with each material having a permittivity of 2 to 5.65 and 31.5 to 61. The characterized solid materials are Teflon, resin, epoxy glass, urethane, FR4, and ceramic with permittivities 2.00, 3.88, 4.60, 3.24, 4.07, and 5.65. Based on the measurement and calculation of FDR values, the average accuracy and NS obtained are 0.060, 93.63%, and 2.58%. Based on previous work, the calculated permittivity for ethanol concentrations of 30%, 50%, and 70% are 61, 47, and 31.5. Based on the measurement and calculation of FDR values, the obtained average accuracy and NS are 0.014, 97.41%, and 0.30%.

In previous work [20], the designed microwave sensor has a curved-feed CSRR-based resonator structure with a resonant frequency of 2.5 GHz for the characterization of solid materials with a permittivity of 1.0006 to 4.4. The characterized solid materials are air, Roger 5880, Roger 4350, and FR4 with permittivities of 1.0006, 2.2, 3.66, and 4.4, respectively. Based on the measurement and calculation of FDR values, the average accuracy and NS obtained are 0.095, 99.77%, and 0.761%.

In previous work [21], the designed microwave sensor has a resonator structure based on tweaking ELC resonators with a resonant frequency of 0.82 GHz for the characterization of vacuum solid materials with permittivity 1 to 10. Based on the measurement and calculation of FDR values, the average accuracy and NS obtained are 0.012, 96.72%, and 1.492%.

Compared to previous works, the proposed sensor demonstrates a unique advantage by being capable of detecting both solid and biological materials, specifically solid meat, which is rarely addressed in earlier studies. In addition, it operates at a lower resonant frequency (0.86 GHz), which is advantageous for sensing biological materials due to improved penetration depth and interaction with high-loss samples. Unlike many previous designs that involve high structural complexity, this work employs a simplified structure based on the combination of CSRR and ELC resonators. This results in a low-cost and practical solution while maintaining acceptable performance metrics such as accuracy and noise stability, making it suitable for real-world applications involving low-frequency biological material detection.

TABLE 8. Comparison with previous research.

Ref	Model	Port	SUT	Range of ε_r	f_r (GHz)	Parameters			Compatibility with Low Frequency	Capability for biological materials	Design complexity
						FDR (GHz)	Accuracy (%)	NS (%)			
[9]	U-shaped resonator	Single	Solid	$1 \sim 4.3$	1.21 2.10	0.009 0.043	99.02 96.44	0.761 1.150	No	No	High
[10]	Triple-rings CSRR	Dual	Semi-solid	1–78.4	2.5	0.042	96.00	0.003	No	No	High
[19]	Double Split Ring Resonator	Dual	Solid and Liquid	2–5.65 31.5–61	2.45	0.060 0.014	93.63 97.41	2.58 0.30	No	No	High
[20]	Curve-feed CSRR	Dual	Solid	1–4.4	2.5	0.095	99.77	1.072	No	No	High
[21]	Tweaking ELC resonator	Dual	Solid	1–10	0.82	0.012	96.72	1.492	Yes	No	Low
This work	**CSRR and ELC**	**Dual**	**Solid Meat**	**1–9.8**	**0.86**	**0.019**	**96.69**	**0.202**	**Yes**	**Yes**	**Low**

6. CONCLUSION

A low-frequency microwave sensor with a simple planar structure based on CSRR and ELC has been successfully developed and validated. The design focuses on ease of fabrication and practical implementation, while enabling effective permittivity detection of various materials, including biological samples. Operating at 0.86 GHz, the sensor provides the advantage of deeper field interaction in lossy biological media, which is essential for reliable material characterisation. Based on measurement result, the proposed sensor has a high performance with accuracy of 96.69%, normalized sensitivity of 0.202%, and FDR of 0.019 GHz. The proposed sensor has a combination of low-frequency operation, high performance, and simple structure that can be a promising solution for practical applications in biological and dielectric material evaluation.

ACKNOWLEDGEMENT

This work is supported by Research and Community Services Institute of Universitas Trisakti and Ministry of Research, Technology and Higher Education of Republik Indonesia through a competitive research grant under the Regular Fundamental Research Scheme fiscal year of 2025 with contract number of 124/C3/DT.05.00/PL/2025 and 1014/LL3/AL.04/2025.

REFERENCES

[1] Al-Behadili, A. A., I. A. Mocanu, N. Codreanu, and M. Pantazica, "Modified split ring resonators sensor for accurate complex permittivity measurements of solid dielectrics," *Sensors*, Vol. 20, No. 23, 6855, 2020.

[2] Fahmy, H. M., H. I. Helmy, F. E. Ali, N. E. Motei, and M. S. Fathy, "Industrial applications of sensors," in *Handbook of Nanosensors: Materials and Technological Applications*, 1–34, Springer, 2023.

[3] Alahnomi, R. A., Z. Zakaria, E. Ruslan, S. R. A. Rashid, and A. A. M. Bahar, "High-Q sensor based on symmetrical split ring resonator with spurlines for solids material detection," *IEEE Sensors Journal*, Vol. 17, No. 9, 2766–2775, May 2017.

[4] Yeo, J. and J.-I. Lee, "High-sensitivity microwave sensor based on an interdigital-capacitor-shaped defected ground structure for permittivity characterization," *Sensors*, Vol. 19, No. 3, 498, 2019.

[5] Morales-Lovera, H.-N., J.-L. Olvera-Cervantes, A.-E. Perez-Ramos, A. Corona-Chavez, and C. E. Saavedra, "Microstrip sensor and methodology for the determination of complex anisotropic permittivity using perturbation techniques," *Scientific Reports*, Vol. 12, No. 1, 2205, 2022.

[6] Royo, I., R. Fernández-García, and I. Gil, "Microwave resonators for wearable sensors design: A systematic review," *Sensors*, Vol. 23, No. 22, 9103, Nov. 2023.

[7] Wang, C., L. Ali, F.-Y. Meng, K. K. Adhikari, Z. L. Zhou, Y. C. Wei, D. Q. Zou, and H. Yu, "High-accuracy complex permittivity characterization of solid materials using parallel interdigital capacitor-based planar microwave sensor," *IEEE Sensors Journal*, Vol. 21, No. 5, 6083–6093, Mar. 2021.

[8] Muñoz-Enano, J., P. Vélez, M. Gil, and F. Martín, "Planar microwave resonant sensors: A review and recent developments," *Applied Sciences*, Vol. 10, No. 7, 2615, Apr. 2020.

[9] Alam, S., Z. Zakaria, I. Surjati, N. A. Shairi, M. Alaydrus, and T. Firmansyah, "Dual-band independent permittivity sensor using single-port with a pair of U-shaped structures for solid material detection," *IEEE Sensors Journal*, Vol. 22, No. 16, 16 111–16 119, Aug. 2022.

[10] Al-Gburi, A. J. A., N. A. Rahman, Z. Zakaria, and M. Palandoken, "Detection of semi-solid materials utilizing triple-rings CSRR microwave sensor," *Sensors*, Vol. 23, No. 6, 3058, Mar. 2023.

[11] Guo, Z., Y. Wang, S. Ke, X. Su, J. Ren, and H. Chen, "1D photonic topological insulators composed of split ring resonators: A mini review," *Advanced Physics Research*, Vol. 3, No. 6, 2300125, Jun. 2024.

[12] Saadat-Safa, M., V. Nayyeri, M. Khanjarian, M. Soleimani, and O. M. Ramahi, "A CSRR-based sensor for full characterization of magneto-dielectric materials," *IEEE Transactions on Microwave Theory and Techniques*, Vol. 67, No. 2, 806–814, Feb.

2019.

[13] Alam, S., I. Surjati, L. Sari, R. D. Mardian, M. Abicha, Z. Zakaria, T. Firmansyah, M. Alaydrus, and Y. Rahayu, "Dual functional liquid displacement and angular detection based on band stop response microwave sensor," *IEEE Access*, Vol. 12, 94 861–94 869, 2024.

[14] Kiani, S., P. Rezaei, and M. Fakhr, "Dual-frequency microwave resonant sensor to detect noninvasive glucose-level changes through the fingertip," *IEEE Transactions on Instrumentation and Measurement*, Vol. 70, 1–8, 2021.

[15] Masrakin, K., S. Z. Ibrahim, H. A. Rahim, S. N. Azemi, P. J. Soh, and S. Tantiviwat, "Microstrip sensor based on ring resonator coupled with double square split ring resonator for solid material permittivity characterization," *Micromachines*, Vol. 14, No. 4, 790, 2023.

[16] Agarwal, S. and M. C. Garg, "Design of an accurate, planar, resonant microwave sensor for testing a wide range of liquid samples," *Electronics*, Vol. 13, No. 22, 4510, Nov. 2024.

[17] Ebrahimi, A., J. Scott, and K. Ghorbani, "Differential sensors using microstrip lines loaded with two split-ring resonators," *IEEE Sensors Journal*, Vol. 18, No. 14, 5786–5793, Jul. 2018.

[18] Abd Rahman, N., Z. Zakaria, R. A. Rahim, M. A. M. Said, A. A. M. Bahar, R. A. Alahnomi, and A. Alhegazi, "High quality factor using nested complementary split ring resonator for dielectric properties of solids sample," *Applied Computational Electromagnetics Society Journal (ACES)*, Vol. 35, No. 10, 1222–1227, 2020.

[19] Jang, S.-Y. and J.-R. Yang, "Double split-ring resonator for dielectric constant measurement of solids and liquids," *Journal of Electromagnetic Engineering and Science*, Vol. 22, No. 2, 122–128, 2022.

[20] Al-Gburi, A. J. A., Z. Zakaria, N. A. Rahman, S. Alam, and M. A. M. Said, "A compact and low-profile curve-feed complementary split-ring resonator microwave sensor for solid material detection," *Micromachines*, Vol. 14, No. 2, 384, Feb. 2023.

[21] Alam, S., I. Surjati, L. Sari, Y. K. Ningsih, M. Y. Fathanah, Y. K. Gultom, G. Daffin, T. Firmansyah, and Z. Zakaria, "UHF-band solid sensor based on tweaking electric field coupled resonator for material characterization," *Progress In Electromagnetics Research M*, Vol. 126, 11–18, 2024.